Waveguide Superlattice-Based Optical Phased Array

Le-Meng Leng, Yue Shao, Pei-Yan Zhao, Guang-Fan Tao, Shi-Ning Zhu, and Wei Jiang*

National Laboratory of Solid State Microstructures, College of Engineering & Applied Sciences, Key Laboratory of Intelligent Optical Sensing and Manipulation (Nanjing University), Ministry of Education, and Collaborative Innovation Center of Advanced Microstructures, Nanjing University, 22 Hankou Road, Nanjing 210093, People's Republic of China

(Received 9 April 2020; revised 24 November 2020; accepted 8 December 2020; published 12 January 2021)

High-density low-crosstalk waveguide superlattices can potentially help shrink the pitch of an optical phased array to half-wavelength, which may lead to superior beam characteristics. While a superlattice's longitudinal coherence is exploited to create phase mismatch and reduce crosstalk, its transverse coherence is also modified and will inevitably disturb the beam forming of the optical phased array. Our theory shows that the transverse and longitudinal coherence can be balanced in a nontrivial superlattice such that superlattice-induced disturbance of the beam can be suppressed without compromising crosstalk. Large supercells less restrained by symmetry offer more degrees of freedom for finding a desirable superlattice structure. The supercell configuration order and structural modulation strength are crucial to balancing coherence and approaching the ideal characteristics of a half-wavelength pitch optical phased array. Experimental results show a high main-beam energy ratio, low sidelobe levels, and a wide angular scanning range. Such optical phased arrays may potentially open up further opportunities for light detection and ranging (LIDAR), wireless optical communications, and biomedical scanning imaging.

DOI: 10.1103/PhysRevApplied.15.014019

I. INTRODUCTION

An optical phased array (OPA) can tilt the wavefront of a light beam emanating from an emitter array by controlling each emitter's phase. This enables nonmechanical beam steering, which may help offer advanced functionality for light detection and ranging (LIDAR), biomedical imaging, and wireless optical communications. According to the principle of phased arrays [1], unless the emitter pitch is less than half-wavelength, the optical phased array may produce secondary beams (called grating lobes). These secondary beams induce unwanted false return signals in LIDAR and biomedical scanning imaging, and severely limit the alias-free scanning range (see Appendix A). These beams also split energy from the main beam, causing serious energy efficiency issues for LIDARs and wireless optical communication [2] applications. In radio-frequency phased arrays, solutions to these problems based on half-wavelength pitch arrays have been available for decades. However, an approach that works well for optical phased arrays remains elusive.

Built upon advances in silicon photonic devices and integration [3–5], silicon-waveguide-based optical phased arrays have aroused significant interest in the last decade [6–16]. Yet reducing emitter pitches to half-wavelength ($\lambda/2$) was not considered a promising direction due to the fundamental issue of high crosstalk in dense waveguides with small pitches. Optical phased arrays with large nonuniform pitches (also called aperiodic arrays) [7,8,12] offer interesting alternatives to disassemble grating lobes; however, the original lobe energy is spread into wide-angle random radiation, forming undesirable background "noise" (Ref. [12] has been able to reduce such "noise" to ≤ -8.9 dB). Waveguide lattices offer intriguing possibilities of manipulating arrays of optical signals [17,18]. Along with related concepts in optical superlattices [19], waveguide lattices may stimulate different thinking for OPAs. Recently, half-wavelength pitch low-crosstalk waveguide arrays have been proposed and demonstrated by introducing a sophisticated waveguide superlattice whose supercell comprises waveguides of different propagation constants [20]. In such a waveguide superlattice, the phase mismatch and *complex multipath interwaveguide couplings* can be precisely controlled according to advanced theory to suppress crosstalk below -20 dB. Using such waveguide superlattices to create half-wavelength pitch optical phased arrays has been proposed [20]. Other interesting approaches of increasing waveguide density have been reported recently also [21–25]. Subsequently, subwavelength-pitch optical phased arrays have received much attention [26–30]. One approach has exploited phase mismatch in a curved waveguide array to suppress crosstalk below -12 dB for a pitch somewhat larger than half-wavelength, leading to an OPA with an

*weijiang@nju.edu.cn

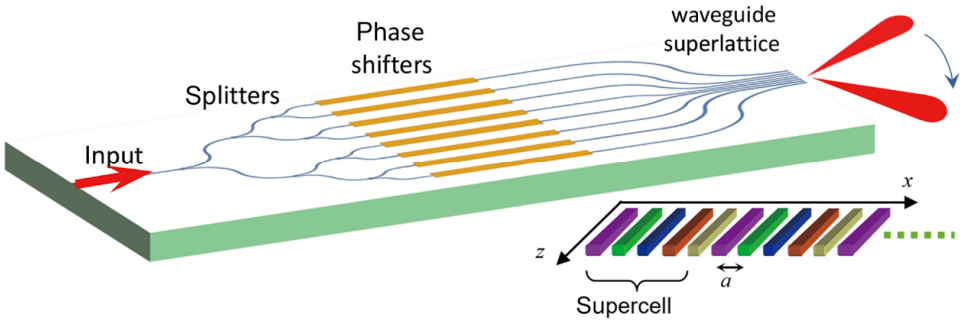

FIG. 1. Schematic drawing of a waveguide-superlattice-based optical phased array. The lower right inset shows the schematic of a waveguide superlattice. Each supercell contains a subarray of waveguides of different widths. A supercell containing n_s waveguides is denoted by SCn_s. Given the waveguide pitch a, the superlattice period is $n_s a$.

alias-free beam steering of $-32°$ to $+32°$ [29]. Although the crosstalk problem can be better solved by a waveguide superlattice, incorporation of a waveguide superlattice in an OPA may lead to some fundamental questions, such as whether the strong structural modulation of a sophisticated superlattice may induce high-level complex background radiation (i.e., certain types of "noise") or spoil the main beam. Preliminary experimental effort [27,31] of constructing an OPA containing a less complicated waveguide superlattice (called SC3 superlattice in Ref. [20]), which works in the moderate crosstalk regime, appeared to show some encouraging beam behaviors. Yet those fundamental questions remain to be fully understood. To answer those questions, the physical mechanism governing the behaviors of a superlattice OPA needs to be expounded to gauge whether the characteristics of a superlattice OPA can fully approach those of an ideal OPA, which generally should have minimal crosstalk. In this work, we explore the fundamental physical mechanism underpinning a waveguide superlattice-based optical phased array. The longitudinal coherence and transverse coherence in the waveguide superlattice govern the crosstalk and beam characteristics of the OPA, respectively. Judicious balance between the longitudinal and transverse coherence is found critical to tailoring the characteristics of a superlattice OPA towards the ideal.

II. THEORY AND ANALYSIS

The schematic of the optical phased array is shown in Fig. 1. Light is split through a series of 1×2 multimode interference couplers, followed by thermo-optic phase shifters with large lateral separations. Then, the light is routed to a half-wavelength pitch waveguide superlattice, which emits light through the waveguide end faces. Hereafter a superlattice with each supercell containing n_s waveguides is denoted by SCn_s. To enable proper function of such a superlattice optical phased array, two aspects are essential: (1) minimize interwaveguide signal crosstalk in the waveguide superlattice; (2) form a coherent beam out of the waveguide superlattice end faces, with minimum departure from the beam of an ideal uniform OPA. To minimize crosstalk in a waveguide superlattice, a rigorous coupled mode theory assisted by Gershgorin circle theorem-inspired analysis is available to suppress *compound* coupling through all possible direct and indirect paths [20,32]. This approach tailors the propagation constants β_n of the waveguide superlattice, which controls the longitudinal coherence along the propagation path (z axis). To understand the mechanism of the superlattice optical phased array whose operation relies on transverse coherence along the x axis, further theoretical insight is required.

To understand the characteristics of a superlattice optical phased array, we focus on a key question: how does the waveguide superlattice modify the beam characteristics from those of an ideal OPA without the superlattice? All modifications stem from the superlattice periodicity and the structure in a supercell. A superlattice OPA with supercell periodicity $n_s a$ generates a Fourier component at a transverse wavevector $k_x = 2\pi m/n_s a$ for integer m, which is expected to produce to a lobe [called "superlattice lobe" here, as illustrated in Fig. 2(a)] at angle $\theta = \arcsin(k_x/k_0)$. This signifies a major type of superlattice-induced disturbance of the radiation characteristics. At the first glance, the superlattice lobe may severely degrade the OPA beam characteristics just like the grating lobes of ordinary OPAs. However, theoretical analysis reveals fundamental differences as we see. Particularly, the superlattice lobe intensity strongly depends on the transverse coherence within a supercell. By proper theoretical treatment, it is possible that the contribution of intrasupercell transverse coherence can be exploited to drastically reduce the superlattice lobe. In this regard, we are encouraged by some phenomena in x-ray diffraction by crystals: some diffraction orders of a compound crystal whose unit cell contains multiple atoms can be annihilated due to destructive coherent contributions from individual atoms in each cell [33]. Hopefully,

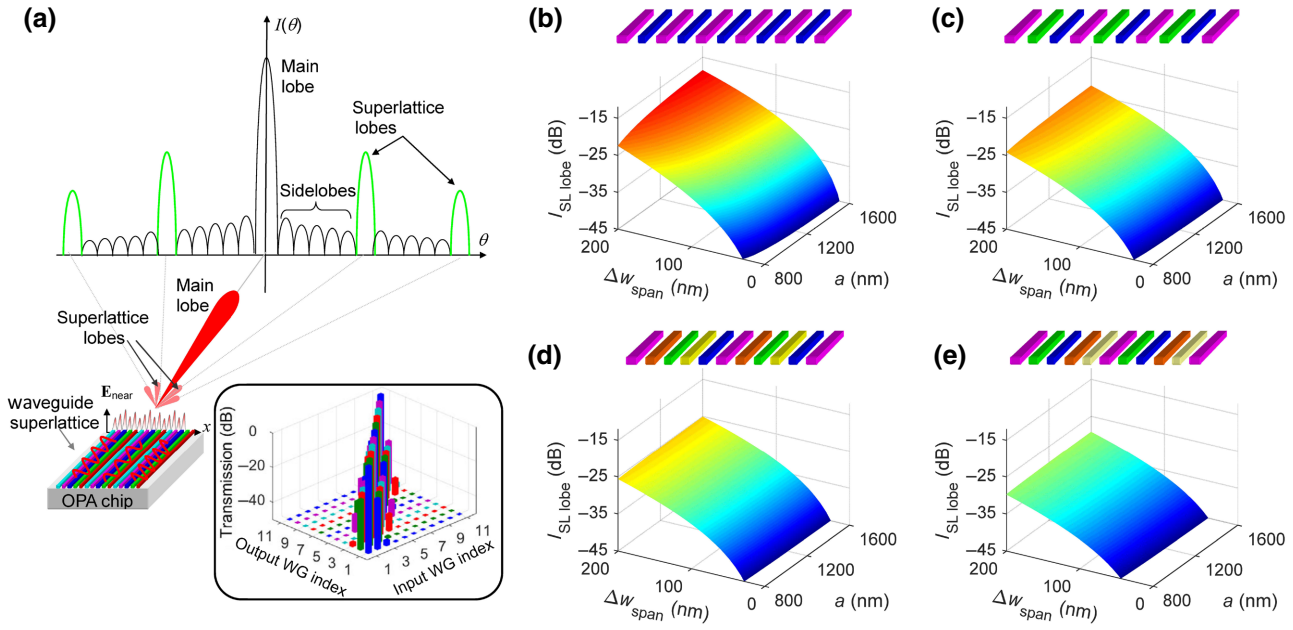

FIG. 2. Waveguide-superlattice-based OPA—theoretical analysis. (a) Schematic illustration of the superlattice lobe. The light field at the OPA output facet produces a beam profile comprising multiple lobes in the far field. Superlattice (SL) lobe levels for optical phased arrays are plotted in (b)–(e) for varying width span Δw_{span} and varying pitch a. The analyzed superlattice structures are (b) SC2, (c) SC3, (d) SC5a, and (e) SC5b. The simulated transmission and maximum crosstalk in a SC5b superlattice with waveguide widths corresponding to $w_{\max} = 480$ nm, and $\Delta w_{\text{span}} = 120$ nm are shown in the lower-right inset of (a), showing all crosstalk < -20 dB ($a = \lambda/2$).

the superlattice lobe can be treated in the same spirit. Of course, whether this idea can be compatible with the low crosstalk requirement of waveguide superlattices is also essential.

For an optical phased array, the far-field wave amplitude is related to the Fourier transform E_F of the emitted field $E_e(x)$ at the output of each emitter, $E_F(k_x) \sim \int E_e(x) \exp(ik_x x)dx$, where x is the transverse coordinate. For an ordinary uniform phased array, the Fourier component for a grating lobe is simply given by

$$E_{F,\text{uni}}(k_x)|_{k_x=2\pi/a} = \sum_{n=0}^{N-1} e^{ik_x na} E_{F,0}(k_x), \tag{1}$$

where $E_{F,0}(k_x)$ and $E_{F,\text{uni}}(k_x)$ are the Fourier transform of an emitter and that of a uniform array with N elements. For a superlattice optical phased array with n_s elements in a supercell, the Fourier transform is given by

$$E_{F,s}(k_x) \sim \sum_{l=0}^{N/n_s-1} e^{ik_x l(n_s a)} \int E_{e,s}(x) \exp(ik_x x)dx, \tag{2}$$

where $E_{e,s}(x)$ is the field in a supercell and we assume that N is sufficiently large so that it is good to approximate N/n_s as an integer (i.e., neglect the small decimal part). If N/n_s is not an integer, there will be residual terms, whose fractional contribution to the far-field beam intensity is on the order of $o[(1/N)^2]$, which is small for sufficiently large N. To illustrate the essential characteristics, we can consider the case where the energy is uniformly distributed over all emitters and the energy within each emitter is uniform over its width. More general cases are discussed later and the results are similar. Then the field of the μ-th emitter is given by $E_{s,\mu} \propto E_{s,0}/\sqrt{w_\mu}$, where $E_{s,0}$ is a normalization constant and w_μ is the width of the μ-th emitter. Therefore, for such a superlattice OPA, the Fourier transform is given by

$$E_{F,s}(k_x) \sim \sum_{l=0}^{N/n_s-1} e^{ik_x l(n_s a)} \times \sum_{\mu=1}^{n_s} \sqrt{w_\mu} E_{s,0} \text{sinc}(k_x w_\mu/2) exp[ik_x a(\mu - 1/2)], \tag{3}$$

where sinc $(x) = \sin(x)/x$, w_μ is the width of the μth emitter in a supercell. Note that the main-beam intensity is proportional to $|E_{F,s}(0)|^2$. The intensity of the superlattice lobe located at $k_x = 2\pi m/n_s a$ is proportional to $|E_{F,s}(2\pi m/n_s a)|^2$. The first-order superlattice lobe is generally the highest. Therefore, it is sufficient to show that the first-order superlattice lobe is low. According to Eq. (2), the Fourier component for the first-order superlattice

lobe can generally be written as

$$E_{F,s}(k_x)|_{k_x=2\pi/(n_s a)} = \sum_{l=0}^{N/n_s-1} e^{ik_x l(n_s a)} \sum_{\mu=1}^{n_s} e^{i\mu k_x a} E_{F,\mu}(k_x), \tag{4}$$

where $E_{F,\mu}(k_x) \sim \sqrt{w_\mu} f_\mu(k_x)$ and $f_\mu(k_x)$ corresponds to the Fourier transform of the μth emitter's normalized field profile [$f_\mu(k_x) = \mathrm{sinc}(k_x w_\mu/2)$ for a uniform profile]. The first sum gives a N/n_s factor. Then it can be readily shown that the normalized first-order superlattice lobe intensity $I_{\mathrm{SL\ lobe}} = |E_{F,s}(2\pi/n_s a)/E_{F,s}(0)|^2$ is given by

$$I_{\mathrm{SL\ lobe}} = \left| \sum_{\mu=1}^{n_s} \sqrt{w_\mu} f_\mu\left(\frac{2\pi}{n_s a}\right) \exp(i2\pi\mu/n_s) / \sum_{\mu=1}^{n_s} \sqrt{w_\mu} f_\mu(0) \right|^2. \tag{5}$$

Obviously, the normalized I_{SLlobe} given here is *independent of the number of supercells* because it only depends on the coherence effect within a single supercell, as represented by the sum of phased terms over μ. The sum of phased terms [$\sim\exp(i2\pi\mu/n_s)$] in Eq. (5) captures the intrasupercell transverse coherence contribution. Figures 2(b)–2(e) shows $I_{\mathrm{SL\ lobe}}$ calculated by Eq. (5) for representative superlattice structures, where Δw_{span} is the waveguide-width span in a superlattice (i.e., the difference between maximum width w_{max} and minimum width w_{min}). For a given Δw_{span}, the waveguides in a SC2 supercell has widths $\{w_{\mathrm{max}}, w_{\mathrm{min}}\}$, the SC3 supercell has widths $\{w_{\mathrm{max}}, w_{\mathrm{min}}+\Delta w_{\mathrm{span}}/2, w_{\mathrm{min}}\}$, the SC5a supercell has widths $\{w_{\mathrm{max}}, w_{\mathrm{min}}+3\Delta w_{\mathrm{span}}/4, w_{\mathrm{min}}+\Delta w_{\mathrm{span}}/2, w_{\mathrm{min}}+\Delta w_{\mathrm{span}}/4, w_{\mathrm{min}}\}$, and the SC5b supercell has widths $\{w_{\mathrm{max}}, w_{\mathrm{min}}+\Delta w_{\mathrm{span}}/2, w_{\mathrm{min}}, w_{\mathrm{min}}+3\Delta w_{\mathrm{span}}/4, w_{\mathrm{min}}+\Delta w_{\mathrm{span}}/4\}$. Here the maximum width is fixed at 480 nm, and w_{min} can be calculated from w_{max} and Δw_{span}. Note that Δw_{span} essentially represents the superlattice's structural modulation strength, and $\Delta w_{\mathrm{span}}=0$ indicates a uniform array without modulation. The SC5b superlattice has the lowest I_{SLlobe} (lower than SC2 and SC3 by up to about 11 dB and about 6.5 dB, respectively). It should be noted that phased arrays often have fairly high requirements for background radiation suppression.

Generally, theory reveals several key guidelines of tailoring the structures in a supercell to harness the transverse coherence and suppress I_{SLlobe}. (i) A superlattice with larger n_s produces more phased terms in the intrasupercell sums over μ in Eq. (5), and offers more degrees of freedom in tailoring transverse coherence to minimize I_{SLlobe}. (ii) For $n_s > 3$, owing to lower superlattice symmetry (of translation and inversion), a SCn_s superlattice may have multiple configurations given the same set of waveguide widths (as in SC5a and SC5b); then the supercell configuration order can also be leveraged to reduce I_{SLlobe}. It is straightforward to see that a SC2 or SC3 superlattice has only one unique configuration after considering all inversion and translation symmetry operations. (iii) Smaller structural modulation strength Δw_{span} is preferred for lower I_{SLlobe}. Indeed, $I_{\mathrm{SLlobe}} \equiv 0$ when $\Delta w_{\mathrm{span}}=0$. However, crosstalk reduction based on longitudinal coherence requires a sufficiently large Δw_{span}. Low crosstalk criterion is approximately related to the superlattice's waveguide widths through coupling matrix $[K]$ elements as (see Appendix B)

$$|\beta(w_m) - \beta(w_n)| >> \sum_{k\neq m} |K_{mk}(w_m, w_k)| + \sum_{k\neq n} |K_{nk}(w_n, w_k)|, \tag{6}$$

where the left-hand side is the phase mismatch between any waveguides m and n in a supercell, and the right-hand side essentially gives an upper bound of the crosstalk contributions from all coupling paths. Obviously, the large phase mismatch required by Eq. (6) implies a large Δw_{span}. Overall, a proper structure needs to balance the longitudinal coherence condition [Eq. (6)] and the transverse coherence influence [Eq. (5)]. Note that as the above coherence-enabled suppression of I_{SLlobe} occurs locally within every single supercell [the sum in Eq. (5) is within a supercell], this effect works for arrays containing just one or a few supercells. Through a holistic study including superlattice-OPA beam characteristics and crosstalk reduction, a SC5b superlattice with $\Delta w_{\mathrm{span}}=120$ nm is chosen. Note that a too wide waveguide may have multiple modes. For a very narrow waveguide, the mode width can expand significantly, which causes stronger crosstalk. Practical aspects such as the single-mode condition for waveguides and fabrication-related issues are also considered in the design. Simulations show all crosstalk channels <-20 dB, as shown in the inset of Fig. 2(a) (see more details of crosstalk simulation in Appendix B). Note that SC2 and SC3 superlattices can have high crosstalk (experimentally measured up to -4 and -10 dB, respectively) as the pitch $a \to \lambda/2$ [20]. Compared to the grating lobe level (typically >-4 dB) of a typical uniform OPA [6,34], the SC5b superlattice lobe can be lower by approximately 25 dB. Note that minimizing the crosstalk through the phase mismatch does not destroy the overall coherence of the OPA system at the output. The fixed phase difference between different paths caused by the superlattice can be easily compensated by adjusting the zero point of the controllable phase shifters of the OPA in experiment (see details in Sec. III). Furthermore, based on Eq. (5), one can readily show $I_{\mathrm{SLlobe}}\neq 0$ when $\Delta w_{\mathrm{span}}\neq 0$ (i.e., the superlattice lobes will inevitably arise as long as $\Delta w_{\mathrm{span}}\neq 0$). Of course, I_{SLlobe} can be suppressed to sufficiently low with proper superlattice structures.

III. EXPERIMENT

Following the theoretical analysis, the structure has been fabricated using CMOS processing technology in a foundry. The top silicon layer and the buried oxide layer have thicknesses of 220 and 2000 nm, respectively. The cover oxide has a total thickness of 3 μm. A TiN heater is used in each thermo-optic phase shifter. The thermo-optic phase shifters are separated laterally by 50 μm. Waveguide bends are used to converge the optical signals from phase shifters to the waveguide superlattice at a small pitch of 800 nm. An OPA testing setup is developed. To test the optical phased array, light from a laser at 1600-nm wavelength is coupled into optical phased array through a grating coupler on chip. Electrical control of the heater is applied through multipin probes on the electrical pads on the chip. To test the beam over a large angular range typically not accessible by a lens due to limited numerical aperture, we can exploit a well-known setup for x-ray diffraction, where a detector is rotated around a sample to arbitrary angles [35]. Here, a photodetector with a small active area is rotated by a mechanical stage to measure the light signal at angles from $-90°$ to $+90°$ in the far field. The testing setup is carefully constructed and calibrated prior to measurement. The different propagation constants of waveguides in the superlattice can introduce unwanted phase difference between different emitters (note that the equivalent path difference is much smaller than the coherence length of the laser, and does not affect the overall coherence of the system). This can be readily compensated (up to a multiple of 2π) by adjusting the zero point of the control signal for each phase shifter. A particle-swarm optimization algorithm [36] is used to find the zero points of the control signals to reach the optimal far-field beam. The grating coupler has a loss of about 5 dB at the OPA operating wavelength. Typical power consumption to achieve π phase shift is about 30 mW, but can be optimized to lower values by introducing isolation trench and other sophisticated structures [37]. The optimization of power consumption is not a focus of this work. Images of a 16-element OPA and waveguide superlattice are shown in Figs. 3(a) and 3(b). The measured far-field beams at representative angles are shown in Fig. 3(c). All beam profiles are normalized by the peak intensity of the 0° beam. No salient grating lobes are present from $-90°$ to $+90°$, which allows for the full field scan. As shown in Fig. 3(d), the peak intensity of the main beam stably follows an envelope function $F_e(\theta)$, and $F_e(\theta)$ can be obtained from the waveguide radiation pattern. At large angles, $F_e(\theta)$ departs substantially from the $\cos^2\theta$ pattern of an ideal dipole radiation. Since $F_e(\theta)$ shows little variation with w, we use $F_e(\theta)$ for $w = 420$ nm (see details in Appendix D). Crosstalk < -20 dB is verified in Fig. 3(e), where the maximum crosstalk over the spectrum of 1520–1600 nm is shown (see more details of crosstalk testing in Appendix B). Note that at most wavelengths, the crosstalk will usually be lower than the maximum value shown here. Also, stray light [20] accounts for a non-negligible background in crosstalk measurement.

The beam profile is analyzed in Fig. 4 to assess the sidelobe level. The theoretical beam profile of a superlattice OPA is very close to that of an ideal uniform OPA

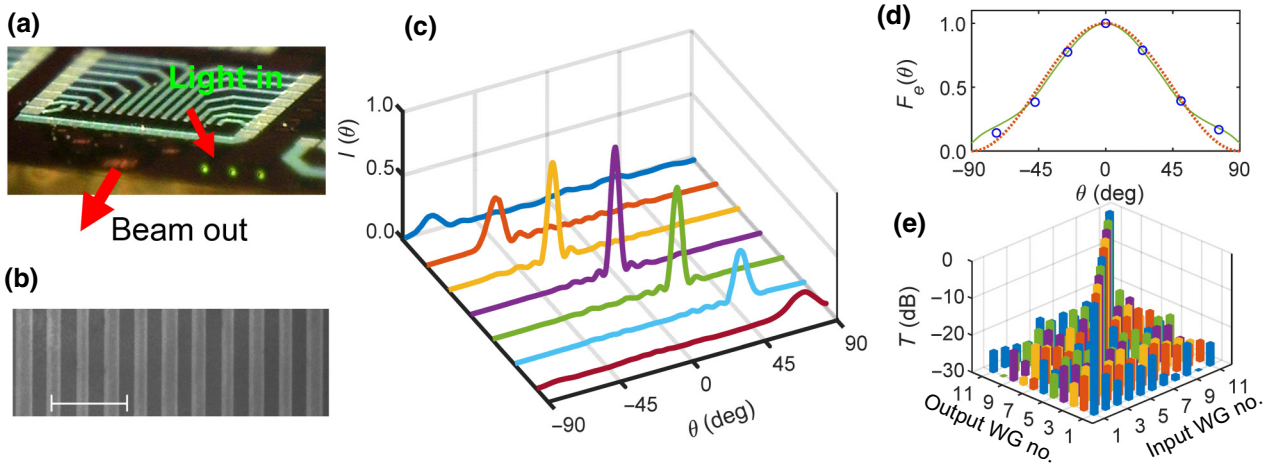

FIG. 3. Experimental result of a SC5b superlattice-based OPA. (a) OPA chip image under an optical microscope. (b) SEM micrograph of a SC5b waveguide superlattice (scale bar: 2 μm), $a = \lambda/2 = 800$ nm (two supercells are shown). (c) Far-field beam characteristics over the whole field for seven representative beams whose main-beam angles are in 25° increments. (d) The envelope function $F_e(\theta)$. Green line, envelope derived from simulated waveguide mode radiation pattern; red dotted line, $\cos^2\theta$. The main-beam intensities [i.e., peak of each beam in (c)] are plotted by blue circles, which follow the envelope function fairly well. (e) Crosstalk characteristics of a SC5b waveguide superlattice measured separately to verify all crosstalk channels < -20 dB.

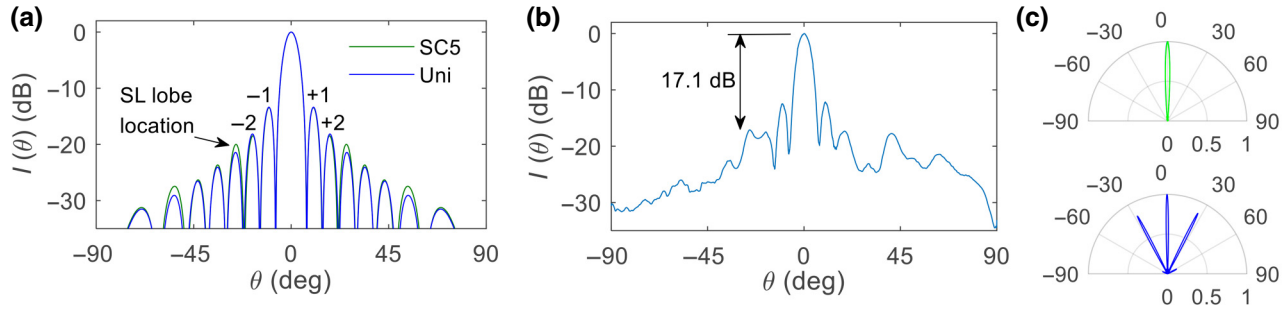

FIG. 4. Beam-profile analysis. (a) Theoretical beam profiles for SC5b superlattice-based OPA at $a = \lambda/2$ (green curve), and ideal uniform OPA (all waveguides having $w = 420$ nm) at $a = \lambda/2$ (blue curve). $F_e(\theta)$ factor included. (b) Experimental result for SC5b superlattice-based OPA. (c) Polar plot of the experimental beam profile of a SC5b OPA with $a = \lambda/2$ (upper panel). As a reference, the experimentally measured beam profile of a uniform OPA with $a = 3.5\,\mu$m (with two salient grating lobes) is shown in the lower panel.

[Fig. 4(a)], except that the first superlattice lobe (approximately 24°) in this particular case overlaps with the third sidelobe and produces a higher composite lobe (approximately −20 dB) by superposition (see detailed discussion of such a superposition in Appendix C). The measured profile in Fig. 4(b) follows the theory result reasonably well, with the secondary lobe levels all below −17.1 dB (except the theory-predicted high ±1 sidelobes, having experimental values <-12.2 dB). The two lowest-order (±1, ±2) sidelobes have around 1-dB degradation compared to the theory values. For reference, the SC5b OPA beam profile is depicted in a polar chart in Fig. 4(c) along with that of a uniform OPA, which exhibits salient grating lobes. The broad bump peaked at $\theta \sim 40°$ in Fig. 4(b) with a relatively low level <-17.8 dB is attributed to weak stray-light scattering and potential fabrication imperfections (roughness, defects, and dust particles may cause light leakage and scattering). Some power unbalance between different emitters due to fabrication imperfection or variation in various parts of the optical waveguide structures is also possible, and may also contribute to the small amount of nonideal background radiation. Theory indicates that the waveguide superlattice approach maintains a high main-lobe energy, with the percentage of area under the main lobe around 91% (differ by $<0.5\%$ from a uniform OPA), and the measured value according to Fig. 4 is about 83%. In contrast, simple calculation shows that this parameter is usually $<50\%$ for uniform OPAs, and $<40\%$ for aperiodic OPAs [7].

IV. DISCUSSIONS

In this proof-of-principle demonstration, we focus on understanding the fundamental principles of superlattice optical phased arrays. The number of elements is limited due to fabrication and testing cost concerns. However, based on the principles demonstrated here, one can readily design and build a superlattice OPA with more elements. As the number of elements increases, the sidelobe level will further decrease; and the superlattice lobe can effectively drop below −30 dB (see Appendix C), and the beam width will decrease (for better angular resolution). Large-scale OPA integration of a record number of elements with flip-chip CMOS circuits has been reported very recently [38]. Note that the high ±1-order sidelobes can be suppressed readily by nonuniform "illumination" (i.e., unequal power between emitters) [39]. Also, gratings or 3D structures can be incorporated to enable 2D beam steering [6,40–42]. The detailed study of these known techniques in (optical) phased arrays is beyond the scope of this work. Recently, an OPA with advanced multipass phase shifters has achieved low heating power consumption with an emitter pitch of 1.3 μm and angular steering range up to 70° [16]. Note that the transverse coherence used to suppress I_{SLlobe} occurs locally in every single supercell. Hence it is not necessary to use many supercells to show its effect. A partial supercell only slightly changes the lobe level by approximately $o[(1/N)^2]$ as discussed in Sec. II.

Note that preliminary experimental effort on a SC3 superlattice-based OPA [27], which explores a moderate crosstalk regime of waveguide superlattices, appears to show an encouraging angular scanning range. The main lobe energy ratio is 72% and peak-to-sidelobe ratio is 11.4 dB for the SC3 OPA [27] [or 63% and 11.4 dB in a related conference paper [31], where the beams cover the left half-field ($\theta \leq 0°$)]. In principle how the superlattice structure may modify the beam properties remains to be fully understood. Here the fundamental characteristics of a superlattice OPA are theoretically analyzed to show that balanced longitudinal and transverse coherence is critical to minimizing the superlattice lobe while suppressing crosstalk, and the roles of supercell configuration and structural modulation are revealed. The

SC5b superlattice-based OPA, which works in the low crosstalk regime (experimentally verified), has the main-beam intensity following the envelope quite well. The main-lobe energy ratio of 83% and peak-to-sidelobe ratio of 12.2 dB of the SC5b OPA appear more beneficial.

Note that the superlattice OPA approach can be easily generalized to other illumination conditions. For nonuniform illuminations, many schemes can possibly be applied to adapt the superlattice OPA approach. Here we discuss a simple example of a Gaussian illumination. For silicon-waveguide-based OPA of N elements, if the optical power weights of the waveguides follow a Gaussian profile, this is essentially a discrete approximation of the Gaussian with N steps. For a superlattice OPA with n_s waveguides in a supercell, a simple adaption would be to let each waveguide in any given supercell carry the same optical power weight, whereas the optical power weights of different supercells follow a Gaussian profile. This is equivalent to a discrete approximation of the Gaussian with N/n_s steps. One can readily show that in this case, Eq. (4) is modified to

$$E_{F,s}(k_x)|_{k_x=2\pi/(n_s a)} = \left[\sum_{l=0}^{N/n_s-1} g_l e^{ik_x l(n_s a)}\right] \left[\sum_{\mu=1}^{n_s} e^{i\mu k_x a} E_{F,\mu}(k_x)\right], \quad (7)$$

where g_l is an illumination factor for the lth supercell (note that this equation is not limited to the Gaussian profile). For a Gaussian, $g_l \sim \exp(-c_g l^2)$ and c_g is a constant determined by the Gaussian width. In Eq. (7), the second term is the intrasupercell sum [same as the second sum in Eq. (4)]; and the first sum is over different supercells. Because in any given supercell, each waveguide carries the same power weight, these two sums are completely decoupled as shown in Eq. (7), which greatly simplifies subsequent calculations. One readily shows that as long as $N/n_s > 20$, the difference of the beam profile between a N-step Gaussian OPA and a N/n_s-step Gaussian superlattice OPA is very small. Other more sophisticated schemes are also possible, more detailed discussion is beyond the scope of this work.

Note that the OPA characteristics obtained here may also benefit other aspects of related applications. For example, a LIDAR may have a limited detection distance due to insufficient signal levels at a long distance. Similarly, wireless optical communications may have limited communication distances or limited bandwidth due to weak signals at long distances. Increase of the laser source power can alleviate this problem, but this may entail higher power consumption and generally higher cost and larger sizes for the laser module. The boost of the main-beam energy ratio of OPA means that these applications can now increase the beam power without requiring a higher-power laser, thereby effectively enhancing the signal level and/or bandwidth and expanding the detection or communication distance.

V. CONCLUSION

In summary, we explore the fundamental physical mechanism governing the behaviors of a waveguide-superlattice-based optical phased array theoretically and experimentally. Intrasupercell transverse coherence can be exploited to drastically reduce the superlattice lobes [via Eq. (5)]; and this must be judiciously balanced with the crosstalk reduction via tailoring the longitudinal coherence. Large supercells less restrained by symmetry may offer more degrees of freedom, and the supercell configuration order and structural modulation strength are key factors for the characteristics of a superlattice OPA, as depicted in Fig. 2. The SC5b superlattice significantly surpasses the SC2 and SC3 superlattice in both crosstalk and superlattice lobe levels, and completely avoids the high-level random background radiation and low main-beam energy associated with an aperiodic array. With a wide angular scanning range, low sidelobe levels (<-12.2 dB), and a high main-beam energy ratio up to 83%, a high-density superlattice optical phased array can tailor and combine guided-wave characteristics and free-space radiation characteristics in a balanced way, the results of which may potentially enhance the functionality of solid-state LIDARs in autonomous vehicles, biomedical scanning imaging, and reconfigurable wireless (free-space) optical communications. Furthermore, whereas "monoatomic" or "diatomic" waveguide lattices have been extensively studied [17], the OPA application drives the exploration of a regime of highly sophisticated superlattices (exemplified by the SC5b superlattice) in terms of guided-wave optics and free-space optics. In this structural regime, rich forms of lattice coherence may further unfold in an intriguing way, whose signature may be projected to the far field and offer diverse avenues of moulding the coherent radiation of light. With proper longitudinal and transverse coherence control in a waveguide superlattice, subwavelength-resolution *active* phase control in high-density waveguides can translate into *dynamic* control of radiation unfettered by limitations of traditional approaches (e.g., grating lobe-related aliasing issues of the low-density structures, crosstalk-related limitations of ordinary high-density waveguide structures, or the fixed radiation characteristics of *passive* structures). This helps to offer better control of spatial and dynamic radiation characteristics and may open up fresh opportunities at the interface between guided-wave optics and free-space optics. Further introducing nanostructures [23,43–46] or nonlinearity [17,21,47] may usher in distinct possibilities in high-performance imaging, optical interconnects, and beam-pattern formation. Superoscillatory beams [48] may

also be used complementarily with the superlattice OPA towards subwavelength spot resolution.

ACKNOWLEDGMENTS

The authors are grateful to F.-L. Zhang, L. Zhu, W.-H. Zhang, T. Li, and X.-S. Jiang for helpful discussions. This work is supported in part by National Key R&D Program of China under Grant No. 2017YFA0303704, and National Natural Science Foundation of China under Grant No. 61775094. We also acknowledge partial support from the Fundamental Research Funds for the Central Universities under Grant No. 021314380072.

L.-M.L. and Y.S. contributed equally to this work.

APPENDIX A: OPTICAL PHASED ARRAYS—LIMITATION DUE TO GRATING LOBES

The fundamentals of phased arrays can be found in Ref. [49]. Some key properties are summarized here for quick reference and comparison. The main lobe (0th order lobe) is at an angle θ_0 given by

$$\sin\theta_0 = \Delta\varphi(\lambda/2\pi a), \tag{A1}$$

where a is the emitter pitch, λ the wavelength, and $\Delta\phi$ the phase difference between adjacent emitters. The angles of nth grating lobes are given by

$$\sin\theta_n = \sin\theta_0 + n\lambda/a. \tag{A2}$$

Note that when the main lobe is at $\theta_0 = \arcsin(\lambda/2a)$, -1 order grating lobe is at $\theta_{-1} = -\arcsin(\lambda/2a)$. For an optical phased array with $a > \lambda/2$, the maximum alias-free scanning range is limited by the ± 1 grating lobes to angular range of θ: $-\arcsin(\lambda/2a) \sim +\arcsin(\lambda/2a)$. Therefore, for $a = 2\,\mu$m, the angular range is about 46° (−23°∼+23°).

APPENDIX B: CROSSTALK REDUCTION IN HIGH-DENSITY WAVEGUIDE ARRAYS

To find a desirable waveguide superlattice, one necessary step is to analyze the crosstalk. The basic ideas are briefly summarized here, following the guidelines in Ref. [20]. Note that this work uses a thinner top silicon layer than that used in Ref. [20]. For two waveguides, the crosstalk can be estimated using the well-known asymmetric directional coupler formula based on propagation constant difference and coupling constant κ. The second nearest neighbor and farther neighbors can not be estimated easily by such a simplistic method. Because the overlap integral in the κ calculation will cover the region of the waveguide (nearest neighbor) between the waveguide in questions (for example, κ_{13} integral will be contributed by the region where waveguide 2 exists). Then one can no longer neglect the presence of waveguide 2. Furthermore, the coupling paths also become sophisticated. For example, between waveguide 1 and 4, the paths should include $1 \to 4$ (direct), $1 \to 2 \to 4$, $1 \to 3 \to 4$, and $1 \to 2 \to 3 \to 4$ and so on. The farther the neighbors, the more complicated the paths. To estimate the total coupling amplitude with contribution from all paths, we resort to a criterion based on a rigorous form of coupled mode theory and Gershgorin circle theorem, which considers the sum of contributions (*compound* coupling) from all paths. If the coupling matrix $[K]$ for a waveguide superlattice satisfies the following criterion, then crosstalk between channel m and n is expected to be low

$$|K_{mm} - K_{nn}| >> \sum_{k\neq m} |K_{mk}| + \sum_{k\neq n} |K_{nk}|. \tag{B1}$$

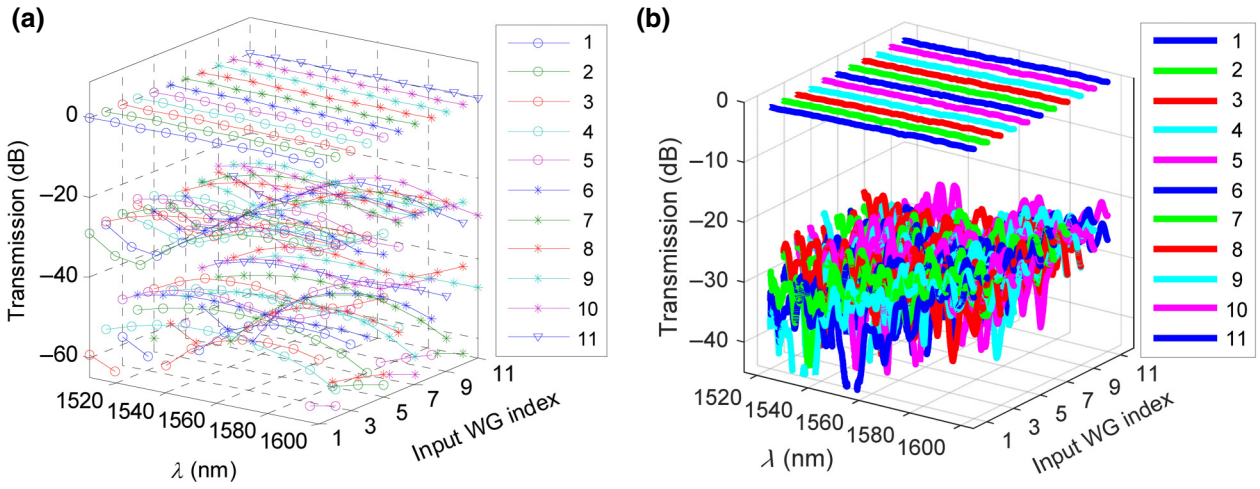

FIG. 5. Crosstalk of a SC5b superlattice for $a = 800$ nm. (a) Simulation; (b) experimental results. Different output channels are marked by different colors.

The right-hand side essentially gives a measure of the maximum compound coupling via all paths. For a low-crosstalk waveguide superlattice, the intermixing of different waveguide modes is very small. In such a structure, it can be shown that the diagonal elements K_{mm} is very close to the propagation constant of the mth waveguide β_m, which depends on the waveguide width w_m. Similarly, the off-diagonal element K_{mk} of a low-crosstalk waveguide superlattice primarily depends on the widths of waveguides m and k. Hence, the above criterion can also be approximately expressed as

$$|\beta(w_m) - \beta(w_n)| >> \sum_{k\neq m} |K_{mk}(w_m, w_k)| + \sum_{k\neq n} |K_{nk}(w_n, w_k)|. \tag{B2}$$

Also, sidewall roughness that is inevitably present in waveguides also plays a dual role. On the one hand, it creates random scattering that may be captured by other waveguides as random crosstalk. On the other hand, it may deter intersupercell coherent crosstalk.

The simulated crosstalk spectra are shown in Fig. 5(a) for a SC5b superlattice ($w_{\max}=480$ nm and $\Delta w_{\text{span}}=120$ nm) with a length of 200 μm in the propagation direction. The measured crosstalk spectra of such a superlattice are shown in Fig. 5(b) (following Ref. [20], only the strongest two or three crosstalk channels for each input waveguide are plotted to avoid a cluttered view). The maximum crosstalk CT(i,j) for each (i,j) is shown in Fig. 3(e). Clearly, all crosstalk channels are below -20 dB.

Note that the waveguide superlattice introduces a very small amount of loss. The total loss of any waveguide in the superlattice is typically around 3.7 dB, which includes edge-coupler loss around 1.4 dB per coupler (by using spot-size conveters and lensed fibers for edge coupling) and waveguide propagation loss for total waveguide length (superlattice part plus the input and output routing waveguide segments) around 3 mm. In principle, the excess loss due to the superlattice structures comprise two parts: input and output coupling loss for connecting to the wider-pitch input-output routing waveguide arrays, and the propagation loss in the waveguide superlattice. Using the shifted-bend coupling structure with sufficiently large bending radii, the input-output coupling loss between the superlattice and wide-pitch waveguides is estimated about 0.1 dB per coupling. The propagation loss of the waveguides is approximately 3 dB/cm for the waveguide with 480 nm width, and <6 dB/cm for the width of 360 nm. Overall, the total excess loss of the waveguide superlattice is fairly small.

APPENDIX C: PRACTICAL ISSUES OF SUPERLATTICE OPA

The analysis of superlattice lobe itself assumes that the number of elements N is sufficiently large. In other words, the result of I_{SLlobe} is rigorous for $N\rightarrow\infty$. As $N\rightarrow\infty$, the sidelobe of an ordinary array vanishes but I_{SLlobe} remains finite. Therefore, I_{SLlobe} given in the main text is the purely the superlattice contribution. For an OPA with a limited N, the sidelobe of the array may not be negligible. The superlattice lobe will be superposed on the sidelobe energy, therefore one may observe a composite lobe level higher than the I_{SLlobe} value given by Eq. (5). Generally, the actual intensity at the superlattice lobe location should be no higher than $\left|\sqrt{I_{\text{SL lobe}}}+e^{i\phi}\sqrt{I_{\text{sidelobe}}}\right|^2 \leq \left|\sqrt{I_{\text{SL lobe}}}+\sqrt{I_{\text{sidelobe}}}\right|^2$. To further evaluate the full effect of a waveguide-superlattice-based optical phased array with a finite size N, the beam profile is calculated for $N=16$ and 128 in Fig. 6. Both SC3 and SC5b structures have $w_{\max}=480$ nm, and $\Delta w_{\text{span}}=120$ nm. For convenience, the uniform field within the emitter width is assumed, but similar levels of superlattice lobe and similar trend can be obtained for other field patterns as well.

For $N=16$, because the sidelobe level is not very low, the SL lobe superimposes on one of the sidelobes and slightly raises its magnitude. For $N=128$, because the sidelobes are very low, the SL lobes are closer to their true magnitudes. Clearly, the lobe levels of superlattice OPAs closely follow those of an ideal uniform OPA, except in the regions near the superlattice lobe. In any case, the *effective* superlattice lobe level (usually including sidelobe contribution) decreases as the number of supercells increases. In both cases, the pure contribution of the superlattice lobe (or the lobe increment due to the SL lobe) is lower in the SC5b-based OPA than in the SC3-based OPA. For example in Fig. 6(a), at the SL lobe location of the SC3-based OPA, the composite lobe is obviously higher than the two neighboring sidelobes on the left and right; whereas the SC5b OPA with $N=16$ has much less departure from the uniform OPA sidelobe profiles. Note that the SC3 superlattice can exhibit moderate crosstalk (up to -10 dB experimentally [20]) for the third nearest neighbors when the pitch approaches half-wavelength. Such crosstalk can induce extra background radiation or unexpected beam behavior. Optical phased arrays based on the SC3 superlattice or similar structures may be explored; but it remains unclear how to develop a technique to overcome moderate or high crosstalk in these structures and minimize its impact on large-scale OPAs, where half-wavelength pitch waveguide arrays may have long copropagating lengths. Furthermore, structure optimization for crosstalk reduction in these structures must be considered together with the accompanying impact on the superlattice lobes and the main beam. In the SC5b superlattice-based OPA, both the

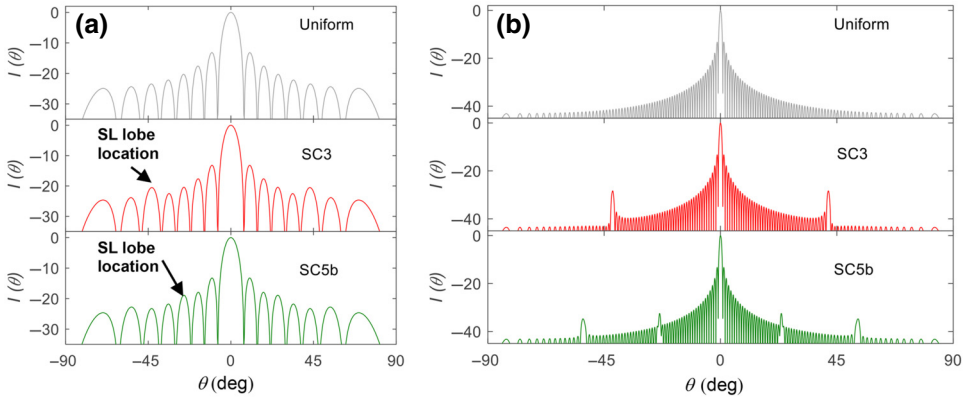

FIG. 6. Simulations results for the array characteristics of optical phased arrays. For OPAs based on SC3, SC5b superlattices, or uniform waveguide arrays, with number of elements: (a) 16; (b) 128. The superlattice lobes appear at the same angles in (a) and (b).

waveguide crosstalk and superlattice lobes can be minimized to approach the ideal characteristics of a λ/2-pitch OPA including the beam envelope. Without the waveguide superlattice, the angular scanning ranges of silicon OPAs are usually limited to ≤100°, with the main lobe energy ratio usually not experimentally measured.

Note that the waveguide pitches (i.e., center-to-center distance, $a = 800$ nm here) can usually be quite accurately defined (with random variation $<\sim 2$ nm) in modern fabrication processes, hence this generally has very small effects on the OPA performance. The waveguide thickness (i.e., the thickness of the SOI layer) could simultaneously increase or decrease by around 10 nm from the nominal value. Such a simultaneous change has little effect on the OPA performance as well. To illustrate the scale of the variation magnitude, the relative variation of the sidelobe levels under the variation of pitch and thickness are calculated and shown in Fig. 7 for representative sidelobes. One hundred random pitch variation configurations are included to obtain the statistical mean and standard deviation of the sidelobe levels. The sidelobe level change ΔI_{lobe} is calculated with respect to the sidelobe level of a SC5b OPA with no pitch and thickness variation. Generally, variation of all sidelobes levels are within ±2%; the lower order sidelobes (which matter the most) as illustrated in Fig. 7 have variation around ±1% (all I_{lobe} calculated in dB, hence ±1% variation of $I_{\text{lobe}} = -20$ dB means ±0.2 dB).

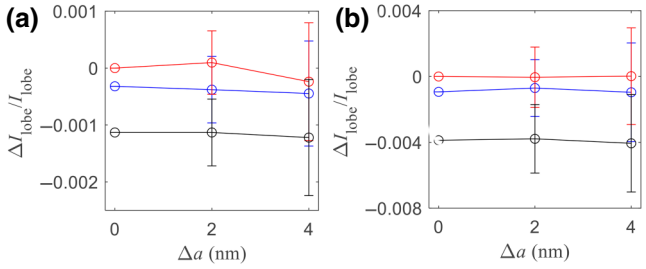

FIG. 7. Variation of the representative sidelobe levels of a SC5b OPA for various value of maximum random variation of pitch Δa, and for different waveguide thicknesses: 210 (blue), 220 (red), 230 (black). (a) ±1-st sidelobes (highest sidelobes); (b) ±3-rd sidelobes (which comprises superlattice lobe contribution).

APPENDIX D: EMITTER RADIATION PATTERN FROM A WAVEGUIDE END FACE

For an ordinary uniform optical phased array with pitch a, the far-field profile is given by

$$I(\theta) = I_0 F_e(\theta)\left[\frac{\sin(N\pi a \sin\theta/\lambda + N\varphi/2)}{\sin(\pi a \sin\theta/\lambda + \varphi/2)}\right]^2, \quad \text{(D1)}$$

where $F_e(\theta)$ is an envelope function, determined by the angular radiation pattern of the emitter. An ideal dipole emitter has the angular radiation pattern of $\cos^2\theta$ [50]. Light emitted from the end face of a waveguide will generate a different pattern in the far field. We simulate the radiation fields from a waveguide using the finite-difference time-domain (FDTD) technique. The radiation field from the endface of a 480-nm-wide waveguide is

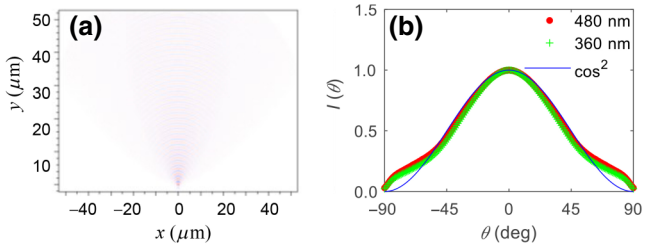

FIG. 8. Waveguide emission pattern. (a) FDTD simulated field for $w = 480$ nm. (b) Extracted angular radiation profile for waveguides of widest and narrowest widths, compared to the simple $\cos^2\theta$ pattern of an ideal dipole.

shown in Fig. 8(a). The envelope function $F_e(\theta)$ can then be extracted from the FDTD simulation results. The extracted $F_e(\theta)$ of the widest and narrowest waveguides in the SC5b superlattice are plotted in Fig. 8(b). Obviously, these two curves are very close. At angles $<60°$, they closely follow $\cos^2\theta$, the radiation pattern of an ideal dipole quite well. However, at larger angles, they deviate significantly from the $\cos^2\theta$ shape.

[1] R. T. Chen and Z. Fu, Optical true-time delay control systems for wideband phased array antennas, Prog. Opt. **41**, 283 (2000).

[2] H. Nikkhah, K. Van Acoleyen, and R. Baets, Beam steering for wireless optical links based on an optical phased array in silicon, Ann. Telecommun. **68**, 57 (2012).

[3] R. Soref, The past, present, and future of silicon photonics, IEEE J. Sel. Top. Quantum Electron. **12**, 1678 (2006).

[4] C. Sun, et al., Single-chip microprocessor that communicates directly using light, Nature **528**, 534 (2015).

[5] Y. Shen, N. C. Harris, S. Skirlo, M. Prabhu, T. Baehr-Jones, M. Hochberg, X. Sun, S. Zhao, H. Larochelle, D. Englund, and M. Soljacic, Deep learning with coherent nanophotonic circuits, Nat. Photonics **11**, 441 (2017).

[6] K. Van Acoleyen, W. Bogaerts, J. Jagerska, N. Le Thomas, R. Houdre, and R. Baets, Off-chip beam steering with a one-dimensional optical phased array on silicon-on-insulator, Opt. Lett. **34**, 1477 (2009).

[7] A. Hosseini, D. Kwong, Y. Zhao, Y.-S. Chen, F. Crnogorac, R. F. W. Pease, and R. T. Chen, Unequally spaced waveguide arrays for silicon nanomembrane-based efficient large angle optical beam steering, IEEE J. Sel. Top. Quantum Electron. **15**, 1439 (2009).

[8] D. Kwong, A. Hosseini, Y. Zhang, and R. T. Chen, 1(12 unequally spaced waveguide array for actively tuned optical phased array on a silicon nanomembrane, Appl. Phys. Lett. **99**, 051104 (2011).

[9] J. K. Doylend, M. J. R. Heck, J. T. Bovington, J. D. Peters, L. A. Coldren, and J. E. Bowers, Two-dimensional free-space beam steering with an optical phased array on silicon-on-insulator, Opt.Express **19**, 21595 (2011).

[10] J. Sun, E. Timurdogan, A. Yaacobi, E. S. Hosseini, and M. R. Watts, Large-scale nanophotonic phased array, Nature **493**, 195 (2013).

[11] C. T. DeRose, R. D. Kekatpure, D. C. Trotter, A. Starbuck, J. R. Wendt, A. Yaacobi, M. R. Watts, U. Chettiar, N. Engheta, and P. S. Davids, Electronically controlled optical beam-steering by an active phased array of metallic nanoantennas, Opt. Express **21**, 5198 (2013).

[12] D. N. Hutchison, J. Sun, J. K. Doylend, R. Kumar, J. Heck, W. Kim, C. T. Phare, A. Feshali, and H. Rong, High-resolution aliasing-free optical beam steering, Optica **3**, 887 (2016).

[13] D. Kwong, A. Hosseini, J. Covey, X. Xiaochuan, Z. Yang, S. Chakravarty, and R. T. Chen, Corrugated waveguide-based optical phased array with crosstalk suppression, IEEE Photonics Technol. Lett. **26**, 991 (2014).

[14] C. V. Poulton, A. Yaacobi, D. B. Cole, M. J. Byrd, M. Raval, D. Vermeulen, and M. R. Watts, Coherent solid-state LIDAR with silicon photonic optical phased arrays, Opt. Lett. **42**, 4091 (2017).

[15] S. Chung, H. Abediasl, and H. Hashemi, A monolithically integrated large-scale optical phased array in silicon-on-insulator CMOS, IEEE J. Solid State Circuits **53**, 275 (2018).

[16] S. A. Miller, Y.-C. Chang, C. T. Phare, M. C. Shin, M. Zadka, S. P. Roberts, B. Stern, X. Ji, A. Mohanty, O. A. J. Gordillo, U. D. Dave, and M. Lipson, Large-scale optical phased array using a low-power multi-pass silicon photonic platform, Optica **7**, 3 (2020).

[17] D. N. Christodoulides, F. Lederer, and Y. Silberberg, Discretizing light behaviour in linear and nonlinear waveguide lattices, Nature **424**, 817 (2003).

[18] H. S. Eisenberg, Y. Silberberg, R. Morandotti, and J. S. Aitchison, Diffraction Management, Phys. Rev. Lett. **85**, 1863 (2000).

[19] S. Zhu, Y. Y. Zhu, and N. B. Ming, Quasi-phase-matched third-harmonic generation in a quasi-periodic optical superlattice, Science **278**, 843 (1997).

[20] W. Song, R. Gatdula, S. Abbaslou, M. Lu, A. Stein, W. Y. C. Lai, J. Provine, R. F. W. Pease, D. N. Christodoulides, and W. Jiang, High-density waveguide superlattices with low crosstalk, Nat. Commun. **6**, 7027 (2015).

[21] M. Mrejen, H. Suchowski, T. Hatakeyama, C. Wu, L. Feng, K. O'Brien, Y. Wang, and X. Zhang, Adiabatic elimination-based coupling control in densely packed subwavelength waveguides, Nat. Commun. **6**, 7565 (2015).

[22] K. Chen, S. Wang, S. Chen, S. Wang, C. Zhang, D. Dai, and L. Liu, Experimental demonstration of simultaneous mode and polarization-division multiplexing based on silicon densely packed waveguide array, Opt. Lett. **40**, 4655 (2015).

[23] B. Shen, R. Polson, and R. Menon, Increasing the density of passive photonic-integrated circuits via nanophotonic cloaking, Nat. Commun. **7**, 13126 (2016).

[24] Y. Bian, Q. Ren, L. Kang, Y. Qin, P. L. Werner, and D. H. Werner, Efficient cross-talk reduction of nanophotonic circuits enabled by fabrication friendly periodic silicon strip arrays, Sci. Rep. **7**, 15827 (2017).

[25] S. Jahani, S. Kim, J. Atkinson, J. C. Wirth, F. Kalhor, A. Al Noman, W. D. Newman, P. Shekhar, K. Han, V. Van, R. G. DeCorby, L. Chrostowski, M. Qi, and Z. Jacob, Controlling evanescent waves using silicon photonic all-dielectric metamaterials for dense integration, Nat. Commun. **9**, 1893 (2018).

[26] M. R. Kossey, C. Rizk, and A. C. Foster, End-fire silicon optical phased array with half-wavelength spacing, APL Photonics **3**, 011301 (2018).

[27] C. T. Phare, M. C. Shin, S. A. Miller, B. Stern, and M. Lipson, arXiv:1802.04624 (2018).

[28] Y. Zhang, Y. Ling, K. Zhang, C. M. Gentry, D. Sadighi, G. Whaley, J. Colosimo, P. Suni, and S. J. B. Yoo, Sub-wavelength-pitch silicon-photonic optical phased array for large field-of-regard coherent optical beam steering, Opt. Express **27**, 1929 (2019).

[29] W. Xu, L. Zhou, L. Lu, and J. Chen, Aliasing-free optical phased array beam-steering with a plateau envelope, Opt. Express **27**, 3354 (2019).
[30] R. Amin, R. Maiti, J. K. George, X. Ma, Z. Ma, H. Dalir, M. Miscuglio, and V. J. Sorger, A lateral MOS-capacitor-enabled ITO mach-zehnder modulator for beam steering, J. Lightwave Technol. **38**, 282 (2020).
[31] C. T. Phare, M. C. Shin, J. Sharma, S. Ahasan, H. Krishnaswamy, and M. Lipson, in *Technical Digest of Conference on Lasers and Electro-Optics (CLEO)*, SM3I.2 (San Jose, CA, USA, 2018).
[32] N. Yang, H. Yang, H. Hu, R. Zhu, S. Chen, H. Zhang, and W. Jiang, Theory of high-density low-cross-talk waveguide superlattices, Photonics Res. **4**, 233 (2016).
[33] C. Kittel, *Introduction to Solid State Physics*, 8th ed. (John Wiley & Sons, New York, 2005).
[34] D. Kwong, A. Hosseini, J. Covey, Y. Zhang, X. Xu, H. Subbaraman, and R. T. Chen, On-chip silicon optical phased array for two-dimensional beam steering, Opt. Lett. **39**, 941 (2014).
[35] B. D. Cullity (ed.), *Elements of X-Ray Diffraction* (Addison-Wesley, Reading, MA, 1967).
[36] S. Abbaslou, R. Gatdula, M. Lu, A. Stein, and W. Jiang, Ultra-short beam expander with segmented curvature control: The emergence of a semi-lens, Opt. Lett. **42**, 4383 (2017).
[37] P. Sun and R. M. Reano, Submilliwatt thermo-optic switches using free-standing silicon-on-insulator strip waveguides, Opt. Express **18**, 8406 (2010).
[38] C. V. Poulton, M. J. Byrd, B. Moss, E. Timurdogan, R. Millman, and M. R. Watts, in Conference on Lasers and Electro-Optics (CLEO), JTh4A.3 (San Jose, CA, 2020).
[39] E. Brookner (ed.) *Practical Phased Array Antenna Systems* (Artech House, Norwood, MA, 1991).
[40] A. Hosseini, D. Kwong, Y. Zhang, S. A. Chandorkar, F. Crnogorac, A. Carlson, B. Fallah, S. Bank, E. Tutuc, J. Rogers, R. F. W. Pease, and R. T. Chen, On the fabrication of three-dimensional silicon-on-insulator based optical phased array for agile and large angle laser beam steering systems, J. Vac. Sci. Technol. B **28**, C6O1 (2010).
[41] S. J. B. Yoo, B. Guan, and R. P. Scott, Heterogeneous 2D/3D photonic integrated microsystems, Microsyst. Nanoeng. **2**, 16030 (2016).
[42] W. D. Sacher, Y. Huang, G. Q. Lo, and J. K. S. Poon, Multilayer silicon nitride-on-silicon integrated photonic platforms and devices, J. Lightwave Technol. **33**, 901 (2015).
[43] S. Wang, P. Chieh Wu, V.-C. Su, Y.-C. Lai, M.-K. Chen, H. Yu Kuo, B. H. Chen, Y. Han Chen, T.-T. Huang, J.-H. Wang, R.-M. Lin, C.-H. Kuan, T. Li, Z. Wang, S. Zhu, and D. Ping Tsai, A broadband achromatic metalens in the visible, Nat. Nanotechnol. **13**, 227 (2018).
[44] H. Huang, H. Li, W. Li, A. Wu, X. Chen, X. Zhu, Z. Sheng, S. Zou, X. Wang, and F. Gan, High-Efficiency vertical light emission through a compact silicon nanoantenna array, ACS Photonics **3**, 324 (2016).
[45] A. Davoyan and H. Atwater, Perimeter-Control architecture for optical phased arrays and metasurfaces, Phys.l Rev. Appl. **14**, 024038 (2020).
[46] A. C. Lesina, D. Goodwill, E. Bernier, L. Ramunno, and P. Berini, On the performance of optical phased array technology for beam steering: Effect of pixel limitations, Opt. Express **28**, 31637 (2020).
[47] D. Kip, M. Soljacic, M. Segev, E. Eugenieva, and D. N. Christodoulides, Modulation instability and pattern formation in spatially incoherent light beams, Science **290**, 495 (2000).
[48] H. Wang, L. Shi, G. Yuan, X. S. Miao, W. Tan, and T. Chong, Subwavelength and super-resolution nondiffraction beam, Appl. Phys. Lett. **89**, 171102 (2006).
[49] E. Brookner (ed.), *Practical Phased Array Antenna Systems* (Artech House, Norwood, MA, 1991). P. F. McManamon, T. A. Dorschner, D. L. Corkum, L. J. Friedman, D. S. Hobbs, M. Holz, S. Liberman, H. Q. Nguyen, D. P. Resler, R. C. Sharp, and E. A. Watson, Optical phased array technology, Proceedings of the IEEE 84, 268 (1996).
[50] J. D. Jackson, *Classical Electrodynamics*, 3rd ed. (Wiley, New York, 1998).